CrossMark

J. Fluid Mech. (2016), *vol.* 791, *pp.* 191–213. © Cambridge University Press 2016
doi:10.1017/jfm.2016.57

Experiments in rotating plane Couette flow – momentum transport by coherent roll-cell structure and zero-absolute-vorticity state

Takuya Kawata[1,†] **and P. Henrik Alfredsson**[1]

[1]Linné Flow Centre, KTH Mechanics, Royal Institute of Technology, S-100 44 Stockholm, Sweden

(Received 20 March 2015; revised 8 January 2016; accepted 18 January 2016;
first published online 17 February 2016)

In spanwise rotating plane Couette flow (RPCF) a secondary flow dominated by three-dimensional roll-cell structures develops. At high enough rotation rates the flow exhibits a state of zero absolute vorticity at the centre of the channel, as described by Suryadi *et al.* (*Phys. Rev.* E, vol. 89, 2014, 033003). They suggested that the zero-absolute-vorticity state is caused by the secondary flow motion of the coherent roll-cell structure induced by the Coriolis force. In the present study we focus on the momentum transport caused by the roll-cell structure of laminar RPCF in order to further understand how the zero-absolute-vorticity state is maintained by the coherent roll cells. The flow is studied through stereoscopic particle image velocimetry measurements, which allow both the Reynolds shear stress and the wall shear stress to be quantified and used as measures of the momentum transport across the channel. Various types of roll-cell structures at different system rotation rates and the momentum transport induced by them are investigated, and the processes in which the momentum is transported in the wall-normal direction are discussed based on a displaced-particle argument as well as the production of the Reynolds stresses. It is shown that the wall-normal fluid motion driven by secondary flow of the roll-cell structure induces two different effects on the mean flow which conflict each other, the momentum transport in the wall-normal direction and the Coriolis acceleration, and the zero-absolute-vorticity state is a stable state where these two effects cancel each other.

Key words: nonlinear instability, rotating flows

1. Introduction

Plane Couette flow under spanwise system rotation, referred to as RPCF (rotating plane Couette flow) in the following, is somewhat challenging to realise in experiment, yet is a good test case to study the effect of spanwise system rotation on shear flows because of its geometrical simplicity: plane Couette flow is conceptually the simplest wall shear flow, and the mean flow vorticity is parallel to the spanwise direction and does not change sign across the flow field, unlike pressure-driven channel flow. Depending on the direction of the system rotation, two cases are possible; the case

†Email address for correspondence: kawata@mech.kth.se

https://doi.org/10.1017/jfm.2016.57 Published online by Cambridge University Press

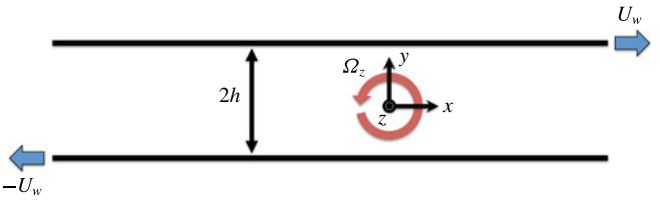


FIGURE 1. (Colour online) Plane Couette flow under spanwise system rotation.

where the system rotation is in the same direction as the mean flow vorticity is called the 'cyclonic' rotation case, while the other case is called the 'anticyclonic' rotation case, and it is well known that the Coriolis force effect is remarkably different between these two cases; it stabilises/destabilises the flow in the cyclonic/anticyclonic case. Bradshaw (1969) pointed out that there is a similarity between flows undergoing spanwise rotation and stratified flows, and the stability can be expressed in the form of a local Richardson number, whereas Kloosterziel, Orlandi & Carnevale (2007) discussed the stability of several different rotating shear flows using numerical simulations.

Theoretically, Lezius & Johnston (1976) showed that the stability equation for RPCF is identical to that for Bernard convection (which has a critical Rayleigh number of 1708). Similarly to Bernard convection RPCF can in the anticyclonic rotation case ($\Omega > 0$) be unstable to spanwise-periodic disturbance, and the neutral stability curve is given as

$$Re_{crit} = \Omega + \frac{107}{\Omega}, \tag{1.1}$$

where $Re = U_w h/\nu$ is the Reynolds number (U_w, h and ν are the wall speed, channel half-width and kinematic viscosity respectively, see figure 1) and Ω is the rotation number, defined as $\Omega = 2\Omega_z h^2/\nu$, with Ω_z being the system rotation rate. The number 107 derives from the Bernard stability problem and is $1708/16 = 106.75 \approx 107$. The lowest critical Reynolds number is $2\sqrt{107} = 20.7$ for $\Omega = 10.3$, and (1.1) shows that at a given Re (> 20.7) the RPCF is unstable when the system rotation rate is in a certain range; for instance, at $Re = 100$ the flow is unstable in the rotation number range $1.08 < \Omega < 98.9$. Hence for a given Reynolds number the flow becomes stable at high rotation rates.

The theoretical results of Lezius & Johnston (1976) predict that a roll-cell structure, regularly spaced in the spanwise direction and straight in the streamwise direction, arises. These two-dimensional and streamwise-independent roll cells were observed through flow visualisation by Tillmark & Alfredsson (1996), Alfredsson & Tillmark (2005), Hiwatashi *et al.* (2007) and Tsukahara, Tillmark & Alfredsson (2010), and planar particle image velocimetry (PIV) by Suryadi, Tillmark & Alfredsson (2013) and Suryadi, Segalini & Alfredsson (2014). Among them, Tsukahara *et al.* (2010) identified 17 different flow states in a wide range of parameters, including both cyclonic and anticyclonic rotations ($-30 \leqslant \Omega \leqslant 30$), and mapped them in the Re–Ω parameter space following Andereck, Liu & Swinney (1986). Suryadi *et al.* (2014) conducted flow visualisations and quantitative velocity measurement by planar PIV at $Re = 100$ up to $\Omega = 100$. These experiments showed that as the rotation number increases the two-dimensional and streamwise-independent roll cells bifurcate to three-dimensional roll cells, such as 'wavy' roll cells and 'twisted' roll cells.

https://doi.org/10.1017/jfm.2016.57 Published online by Cambridge University Press

Some tertiary states corresponding to these experimentally observed structures have also been found numerically (Nagata 1998; Daly *et al.* 2014).

Another interesting characteristic of shear flows for anticyclonic system rotation is the behaviour of the mean absolute vorticity, defined as the sum of the vorticity of the mean flow and twice the system rotation. The coherent roll-cell structure induces additional momentum transport by its secondary motion and remarkably changes the mean flow profile, which may result in a state where the absolute vorticity is zero in the central parts of the channel when the system rotation rate is sufficiently high. This 'zero-absolute-vorticity' state has been observed in numerical simulations of turbulent plane Poiseuille flow (e.g. Kristoffersen & Andersson 1993; Tanaka *et al.* 2000; Xia, Shi & Chen 2016) as well as in RPCF with anticyclonic system rotation (Bech & Andersson 1997). The recent PIV measurements by Suryadi *et al.* (2014) on laminar RPCF at $Re = 100$ showed that the zero-absolute-vorticity state also can appear in this regime, which suggests that the zero absolute vorticity is not caused by the turbulence per se, but may also be due to the secondary flow induced by the roll-cell structures that arise from the Coriolis-force-induced instability.

In the present study we focus on the momentum transport across the channel driven by the roll-cell structure of the laminar RPCF at $Re = 100$ and investigate the mechanism of how the state of zero absolute vorticity is maintained. We expand the experimental set-up employed by Suryadi *et al.* (2014) to stereoscopic PIV measurements in order to obtain all three velocity components, including the wall-normal component. The Reynolds shear stress and the wall shear stress are evaluated based on the PIV measurements as a measure of the additional momentum transport by the roll cells, and their variation with the system rotation rate is investigated. The mechanism of the zero absolute vorticity is discussed, with a focus on the Reynolds stress production as well as the displaced-particle argument.

2. Governing equations

2.1. *Momentum transport equations*

We consider flow between two infinite parallel flat plates moving at constant speeds $\pm U_w$ in the opposite directions under system rotation, as schematically shown in figure 1. The origin of the coordinate system is defined at the centre between the plates, and the x-, y- and z-axes are taken in the streamwise, wall-normal and spanwise directions. We also define $\boldsymbol{e}_1$, $\boldsymbol{e}_2$ and $\boldsymbol{e}_3$ as the unit vectors pointing in the x-, y- and z-directions. The system rotation vector $\boldsymbol{\Omega}$ considered in this study is constant in time and parallel to the z-axis, and is written as $\boldsymbol{\Omega} = \Omega_z \boldsymbol{e}_3$, with Ω_z being the constant system rotation rate. Letting $\tilde{\boldsymbol{u}} = \tilde{u}\boldsymbol{e}_1 + \tilde{v}\boldsymbol{e}_2 + \tilde{w}\boldsymbol{e}_3$ be the velocity vector, one can write the continuity and the momentum conservation equations observed in the rotating frame as

$$\boldsymbol{\nabla} \cdot \tilde{\boldsymbol{u}} = 0, \tag{2.1}$$

$$\rho \left[\frac{\partial \tilde{\boldsymbol{u}}}{\partial t} + (\tilde{\boldsymbol{u}} \cdot \boldsymbol{\nabla})\, \tilde{\boldsymbol{u}} \right] = -\boldsymbol{\nabla} \tilde{p} + \mu \nabla^2 \tilde{\boldsymbol{u}} - 2\rho \Omega_z \boldsymbol{e}_3 \times \tilde{\boldsymbol{u}}, \tag{2.2}$$

where $\tilde{p}$ is the pressure including both the static pressure and the centrifugal acceleration, and ρ and μ are the density and the dynamic viscosity of the fluid respectively, both of which are here assumed to be constant. In the undisturbed laminar flow case, as the flow can be assumed unidirectional ($\tilde{v} = \tilde{w} = 0$ and $\tilde{u}$ depends only on y), one obtains a linear velocity profile:

$$\tilde{u}(y) = \frac{y}{h} U_w. \tag{2.3}$$

https://doi.org/10.1017/jfm.2016.57 Published online by Cambridge University Press

The non-dimensional parameters that characterise the flow under consideration are the Reynolds number and the rotation number, here defined as $Re = U_w h/\nu$ and $\Omega = 2\Omega_z h^2/\nu$ respectively. In some earlier studies a rotation number defined as $Ro = 2\Omega_z h/U_w$ has been used. The relation between these differently defined rotation numbers is $\Omega = Ro\,Re$, and their physical meaning can be interpreted as

$$\Omega = \frac{\text{Coriolis force}}{\text{Viscous force}}, \tag{2.4}$$

$$Ro = \frac{\text{Coriolis force}}{\text{Inertia force}} \tag{2.5}$$

respectively. In the present study we use Ω following the earlier experimental studies by Tsukahara *et al.* (2010) and Suryadi *et al.* (2014).

We consider the moving walls to be infinite in the streamwise and spanwise directions, therefore the mean flow field can be considered to be statistically homogeneous in the x- and z-directions. We define the averaging operation, denoted by $\langle\cdot\rangle$, as taking the average in these directions and in time. We consider a decomposition by which each instantaneous quantity is separated into the averaged value and the deviation:

$$\tilde{\boldsymbol{u}} = \boldsymbol{U} + \boldsymbol{u}, \tag{2.6}$$

$$\tilde{p} = P + p, \tag{2.7}$$

where $\boldsymbol{U} = U\boldsymbol{e}_1 + V\boldsymbol{e}_2 + W\boldsymbol{e}_3$ and P are the averaged velocity vector and pressure respectively, and $\boldsymbol{u} = u\boldsymbol{e}_1 + v\boldsymbol{e}_2 + w\boldsymbol{e}_3$ and p are the deviations of $\tilde{\boldsymbol{u}}$ and $\tilde{p}$ from their averaged values.

Applying the averaging operation to the x-component of (2.2) one can obtain the mean streamwise momentum equation:

$$0 = \frac{\mathrm{d}}{\mathrm{d}y}\left(\mu\frac{\mathrm{d}U}{\mathrm{d}y} - \rho\langle uv\rangle\right), \tag{2.8}$$

where $-\rho\langle uv\rangle$ is the Reynolds shear stress, which represents the effect of the momentum transport by the velocity variation to the mean flow. Equation (2.8) is in the exactly same form as in the case of plane Couette flow without system rotation, as the streamwise Coriolis force $2\Omega_z\tilde{v}$ disappears by the averaging operation since $V = 0$. Equation (2.8) shows that the total shear stress, i.e. the sum of the viscous and the Reynolds shear stresses, is constant across the channel. By integrating (2.8) from either wall to an arbitrary y-position, one obtains

$$\mu\frac{\mathrm{d}U}{\mathrm{d}y} - \rho\langle uv\rangle = \tau_w, \tag{2.9}$$

where τ_w is the wall shear stress. Using the wall velocity U_w and the channel half-width h as the reference scales, one obtains a non-dimensional form of (2.9):

$$\frac{1}{Re}\frac{\mathrm{d}(U/U_w)}{\mathrm{d}(y/h)} - \frac{\langle uv\rangle}{U_w^2} = \frac{\tau_w}{\rho U_w^2} = \left(\frac{u_\tau}{U_w}\right)^2, \tag{2.10}$$

where u_τ is the friction velocity, defined as $u_\tau = \sqrt{\tau_w/\rho}$. Equations (2.9) and (2.10) show that τ_w can be determined from the profiles of U and $\langle uv\rangle$ near the channel

https://doi.org/10.1017/jfm.2016.57 Published online by Cambridge University Press

centre, the measurement of which is obviously easier in practice than a direct measurement of the wall shear stress. It should be noted that one can easily obtain the theoretical value of the wall shear stress in the case of the laminar linear velocity profile:

$$\frac{\tau_w}{\rho U_w^2} = \frac{1}{Re}, \tag{2.11}$$

by substituting (2.3) into (2.10) and assuming $-\langle uv \rangle = 0$.

2.2. *Absolute vorticity and inviscid instability of the RPCF*

In the RPCF the mean flow vorticity has a non-zero component only in the z-direction, and one can define the absolute vorticity as

$$\Omega_a = -\frac{\mathrm{d}U}{\mathrm{d}y} + 2\Omega_z. \tag{2.12}$$

The RPCF has an inviscid instability when the absolute vorticity is in the opposite sign of the background vorticity, i.e. $2\Omega_z\Omega_a < 0$. For the basic linear velocity profile of the RPCF this inviscid instability criterion is written in non-dimensional form as

$$\frac{2\Omega_z\Omega_a}{(U_w/h)^2} = \frac{\Omega}{Re}\left(-1 + \frac{\Omega}{Re}\right) < 0, \tag{2.13}$$

which results in $0 < \Omega/Re < 1$. Therefore, by increasing Ω at a fixed Re one transitions from unstable conditions ($\Omega < Re$) to the state of zero absolute vorticity ($\Omega = Re$) and then to stable conditions ($\Omega > Re$). At low rotation rates there are, of course, also viscous effects that stabilise the flow, which is apparent from (1.1).

2.3. *Reynolds stress transport*

Based on (2.2) one can obtain the transport equation of the Reynolds stresses (per unit mass) $\langle u_i u_j \rangle$ (the procedure to be applied to (2.2) for the derivation is outlined in detail in, for example, Wilcox (1993, pp. 17–18)):

$$\left(\frac{\partial}{\partial t} + U_k\frac{\partial}{\partial x_k}\right)\langle u_i u_j \rangle = P_{ij} + \Pi_{ij} - \varepsilon_{ij} + D_{ij}, \tag{2.14}$$

where the four terms on the right-hand side are the production (P_{ij}), pressure-strain redistribution (Π_{ij}), viscous dissipation (ε_{ij}) and diffusion (D_{ij}) of $\langle u_i u_j \rangle$. The most interesting term in (2.14) is the production term P_{ij}, which represents the production of velocity deviations from the averaged flow and is written as

$$P_{ij} = -\langle u_i u_k \rangle\frac{\partial U_j}{\partial x_k} - \langle u_j u_k \rangle\frac{\partial U_i}{\partial x_k} - 2\Omega_k\left(\epsilon_{ikm}\langle u_j u_m \rangle + \epsilon_{jkm}\langle u_i u_m \rangle\right), \tag{2.15}$$

where ϵ_{lmn} is the permutation tensor. The first two terms of (2.15) represent the Reynolds stress production by the mean velocity gradient, and the other system-rotation-related terms represent the Coriolis-force effect. As the Coriolis force does not perform work, the physical interpretation of this term is energy transfer between different Reynolds stress components (Tsukahara *et al.* 2010).

https://doi.org/10.1017/jfm.2016.57 Published online by Cambridge University Press

In the flow field under consideration in the present study, the Reynolds shear stress components $\langle uw \rangle$ and $\langle vw \rangle$ are considered to be zero due to symmetry, and the transport equations of the other non-zero components can be considerably simplified to become

$$\langle u^2 \rangle: \quad 0 = -2\langle uv \rangle \left(\frac{\mathrm{d}U}{\mathrm{d}y} - 2\Omega_z \right) + \Pi_{11} - \varepsilon_{11} + D_{11}, \tag{2.16}$$

$$\langle v^2 \rangle: \quad 0 = -4\langle uv \rangle \Omega_z + \Pi_{22} - \varepsilon_{22} + D_{22}, \tag{2.17}$$

$$\langle w^2 \rangle: \quad 0 = \Pi_{33} - \varepsilon_{33} + D_{33}, \tag{2.18}$$

$$-\langle uv \rangle: \quad 0 = 2\langle u^2 \rangle \Omega_z + \langle v^2 \rangle \left(\frac{\mathrm{d}U}{\mathrm{d}y} - 2\Omega_z \right) + \Pi_{12} - \varepsilon_{12} + D_{12}. \tag{2.19}$$

As shown, the Reynolds stresses $\langle u^2 \rangle$, $\langle v^2 \rangle$ and $-\langle uv \rangle$ have their production terms associated with the mean velocity gradient and/or the system rotation, while there is no production of $\langle w^2 \rangle$. It should be noted that the Ω_z-related terms in the production of $\langle u^2 \rangle$ and $\langle v^2 \rangle$ are in the exactly same form except the sign, which means that they represent energy transfer between $\langle u^2 \rangle$ and $\langle v^2 \rangle$. Furthermore, the absolute vorticity $\Omega_a = -\mathrm{d}U/\mathrm{d}y + 2\Omega_z$ appears in the production terms in (2.16) and (2.19). Hence, under the state of zero absolute vorticity, the production of $\langle u^2 \rangle$ is zero, which means that the energy from the mean flow to $\langle u^2 \rangle$ is completely transferred to $\langle v^2 \rangle$, and the contribution of $\langle v^2 \rangle$ to the production of $-\langle uv \rangle$ also vanishes. In § 5, a detailed discussion on the flow structure and the mechanism of the zero-absolute-vorticity state will be given based on the Reynolds stress production terms.

3. Experimental set-up and procedure

3.1. *Flow apparatus and measurement conditions*

The experimental flow apparatus has been described in detail elsewhere, see for instance Suryadi *et al.* (2013). In short it is an apparatus in which a plane Couette flow facility designed by Tillmark & Alfredsson (1991, 1992) is mounted on a turntable with a PIV system, as schematically shown in figure 2(*a*), and thus can be rotated around its spanwise axis with an angular velocity of up to 0.58 rad s^{-1}. The countermoving wall of the Couette channel is a thin and endless plastic belt of 0.05 mm thickness and 30 cm width that is driven by two large cylinders located at both ends of the water tank. Both the wall of the water tank and the plastic belt are made of transparent material (glass and polyester respectively), so that optical access to the test section is possible. (The same design idea for the plane Couette flow apparatus has been used by Daviaud, Hegseth & Bergé (1992), Malerud, LØY & Goldburg (1995), Zettner & Yoda (2001), Hagiwara *et al.* (2002) and most recently Couliou & Monchaux (2015); however, RPCF has not been studied in any of these.)

The water tank is filled with water, leaving a few centimetres of the top end of the plastic belt above the free surface, and the motion of the plastic belt in the test section is guided by the vertical glass walls (the glass wall of the water tank and an additional glass plate installed inside the tank, see figure 2*b*). In this way, a thin lubricating water layer is established between the plastic belt and the glass wall surface, and its surface tension forces the belt to move stably along the glass walls. The channel width can be varied by moving the glass plate placed inside the water tank, and the distance between the countermoving belts was measured to be $2h = 19.0 \pm 0.2$ mm using a microscope (for a detailed description of the procedure to measure the wall distance

https://doi.org/10.1017/jfm.2016.57 Published online by Cambridge University Press

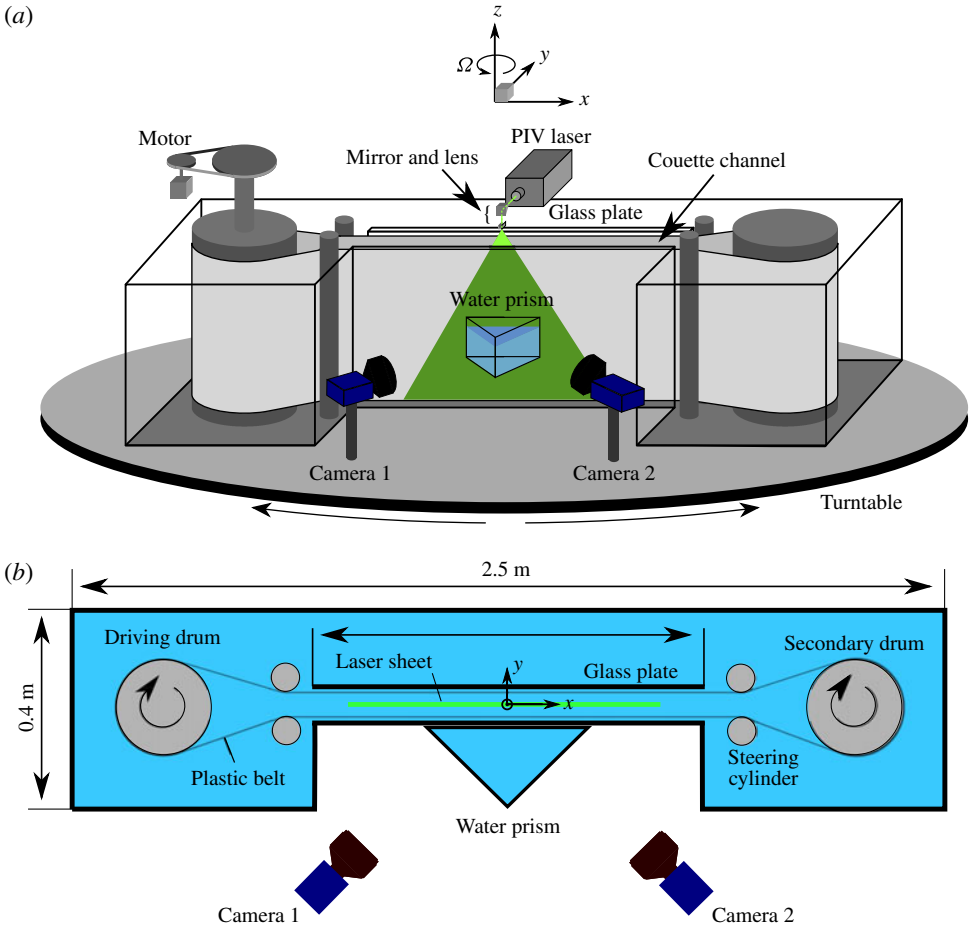


FIGURE 2. (Colour online) Experimental apparatus for rotating plane Couette flow: (*a*) isometric view of the apparatus; (*b*) top view of the test section and camera arrangement.

by a microscope, see, for example, Tsukahara *et al.* (2010)). The active size of the test section of the Couette channel is approximately 1.5×0.28 m^2 in the streamwise and spanwise directions, which corresponds to $156h \times 30h$. The top of the test section is covered by transparent plastic blocks to achieve symmetric boundary conditions between the top and bottom sides in the test section.

In the present experiment the belt speed U_w was kept constant during measurement at a value of approximately 10.6 mm s^{-1} which was chosen according to the temperature of the water (18.8 °C on average), so that the Reynolds number was $Re = 100 \pm 1$ throughout the study. Various rotation numbers in the range of $0 \leqslant \Omega \leqslant 106$ were used; most of the observed Ω values were in the range $1.08 < \Omega < 98.9$, the aforementioned unstable region.

3.2. *Stereoscopic PIV measurement and data acquisition procedure*

Stereoscopic PIV measurements were made using a continuous laser with a wavelength of 532 nm (type MgL-F-532, CNI Optoelectronics Technology) and two 8-bit CCD cameras with a resolution of 1024 × 768 pixel^2 (Genie HM1024, DALSA)

https://doi.org/10.1017/jfm.2016.57 Published online by Cambridge University Press

connected with 24 mm tilt lenses (T-S 24 mm $f/3.5$ ED AS UMC, Samyang). The continuous laser beam was expanded into a laser sheet positioned parallel to the xz-plane by a right-angle prism and a cylindrical lens. The right-angle prism and the cylindrical lens were mounted on a motorised linear traversing unit, so that the laser sheet could be traversed in the y-direction allowing sequential measurements at different y-positions. The viewing angle of the cameras was 45° and the Scheimpflug condition was satisfied by tilting the lenses. There was a laboratory-built water prism attached to the glass wall in front of the test section, in order to reduce image deformation due to refraction in the optical path. The PIV system was mounted on the turntable with the plane Couette flow facility and remotely operated via a wireless network connection from a stationary workstation. Spherical polyamide seeding particles with mean diameter and density of 20 μm and 1.03 g cm^{-3} respectively (PSP-20, Dantec) were used as tracers.

The particle image pairs taken by each CCD camera were processed by a three-step PIV algorithm based on the fast Fourier transform cross-correlation method, in which the basic PIV, the discrete window shift PIV and the central-difference image-correction method (Wereley & Gui 2003) were applied in the first, second and third steps with increasing spatial resolution. The size of the interrogation area was 48×48 pixel^2 in the first and second steps, and 32×32 pixel^2 in the third step, which corresponds to a spatial resolution of 4×3.2 mm^2. The uncertainty in evaluation of the particle displacement by the PIV algorithm was approximately 0.2 pixel, which corresponds to 3 % of U_w in the present experiment. The size of the measurement domain was $8.6h \times 10.6h$ in the x- and z-directions respectively, and there were 42×64 data points with 50 % overlap ratio.

The reconstruction of the three velocity components was conducted using the method proposed by Soloff, Adrian & Liu (1997). The projection functions were approximated by second-order polynomial functions of x, y and z, and the unknown coefficients were determined by calibration. An aluminium plate which had a square grid with a grid spacing of 15 mm on the surface was used as a calibration target, and the calibration images were acquired with the calibration plate located at $y/h = 0$, ± 0.21, ± 0.42 and -0.63.

Stereoscopic PIV measurements were carried out at nine different wall-normal positions, $y/h = 0$, ± 0.19, ± 0.38, ± 0.57 and ± 0.74. The measurements at these different y-positions were made in a sequence going from $y/h = 0.74$ to $y/h = -0.74$. After image acquisition at one measurement location the laser sheet was traversed to the next location by the motorised traversing unit, and then the next image pairs were acquired. This routine was repeated until the image acquisition at the last measurement position $y/h = -0.74$ was finished, and then the laser sheet was traversed back to the initial position, after which the next sequence began. The image pairs were taken with an exposure time of 15 ms and with a temporal interval of 200 ms. Traversing the laser sheet between each measurement position took 2.0 s, and it took 8 s to return from the last measurement position to the initial position; in total one sequence took 28 s. This sequence was repeated 200 times to obtain a sufficient number of samples, and consequently the measurement duration was approximately 1.5 h for each Ω.

3.3. *Flow visualisation*

Visualisations of the coherent roll-cell structure were also made in addition to the stereoscopic PIV measurements. The procedure of the flow visualisation was the same as that described in Suryadi *et al.* (2014). The fluid was seeded by

https://doi.org/10.1017/jfm.2016.57 Published online by Cambridge University Press

titanium-dioxide-coated mica platelets (Iriodin 120 (5–25 μm), Merck), and one of the CCD cameras used for the PIV measurement was used, equipped with a 12 mm lens. The size of the field of view was approximately $40h \times 30h$ in the streamwise and spanwise directions. The acquired images were digitally processed to improve the quality: the same treatment to remove inhomogeneous background light intensity as used in Suryadi *et al.* (2014) was applied to the acquired images, and the contrast was further enhanced using the function '`histeq`', which is available in the MATLAB® library.

4. Results

All results presented were obtained at $Re = 100$, but at different rotation numbers. In § 4.1, the coherent vortex structures at some representative rotation numbers are presented by showing the three-dimensional instantaneous velocity fields together with the corresponding flow visualisation images. Profiles of statistics such as the mean velocity, the absolute vorticity and the Reynolds stresses are given in § 4.2.

4.1. *Coherent roll-cell structures and instantaneous velocity fields*

Snapshots of the roll-cell structure captured by flow visualisation for $\Omega = 1.5$, 8, 20, 55 and 90 are presented in figure 3. Similarly, instantaneous velocity fields measured by stereoscopic PIV are presented in figure 4 (note that figures 3 and 4 were not obtained simultaneously). The red rectangle in each snapshot of figure 3 roughly shows the size and location of the PIV measurement domain, and the colours and the red/black vectors in figure 4 represent the value of the streamwise velocity component $\tilde{u}/U_w$ and the velocity vector with positive/negative wall-normal velocity respectively. For readability, the number of data points shown for the red/black vectors is reduced to 1/4 of the total data points in figure 4(*b–e*), and no red/black vectors are shown in figure 4(*a*) (at $\Omega = 1.5$ the velocity vectors are almost parallel to the xz-plane due to a very small wall-normal velocity component $\tilde{v}$; if shown they cover the xz-plane and the streamwise velocity colour contours cannot be seen).

As shown in figure 3(*a*), the roll-cell structure takes the form of straight streamwise-oriented roll cells at $\Omega = 1.5$, and these two-dimensional roll cells become wavy and some branchings also appear at $\Omega = 8$, as shown in figure 3(*b*). The instantaneous velocity fields shown in figure 4(*a*,*b*) present the corresponding distribution of $\tilde{u}$, indicating that the roll-cell structures shown in figure 3(*a*,*b*) result in a significant variation of the streamwise velocity in the xz-plane. In figure 4(*b*) a branching of the wavy roll cells is also captured. The wavy roll-cell structure observed at $\Omega = 8$ appears to correspond to the tertiary flow found by Nagata (1998) at $R = 400$ and $\Omega = 35$ with their definition of the Reynolds and rotation numbers (these values should be divided by 4 to correspond to the values here). For these parameters Nagata (1998) noted that '... the magnitude of the streamwise velocity on $z = 0$ ($z = y/h$ in the notation of Nagata (1998)) is almost equal to a half of the wall velocity...'. This corresponds fairly well to the maximum measured values (which are $\pm 0.60 U_w$) of the streamwise variation seen for $y/h = 0$ in figure 4(*b*).

At $\Omega = 20$, as shown in figure 3(*c*), the roll-cell structure is again fairly straight in the streamwise direction, which was denoted by Tsukahara *et al.* (2010) as '2Dh' roll cells (two-dimensional roll cells for high Ω), and the corresponding instantaneous velocity is presented in figure 4(*c*). While the roll cells at this rotation number look similar to the two-dimensional roll cells observed at $\Omega = 1.5$, the width of the roll cells is greater, and the important difference is that the 2Dh roll cells at $\Omega = 20$ induce

https://doi.org/10.1017/jfm.2016.57 Published online by Cambridge University Press

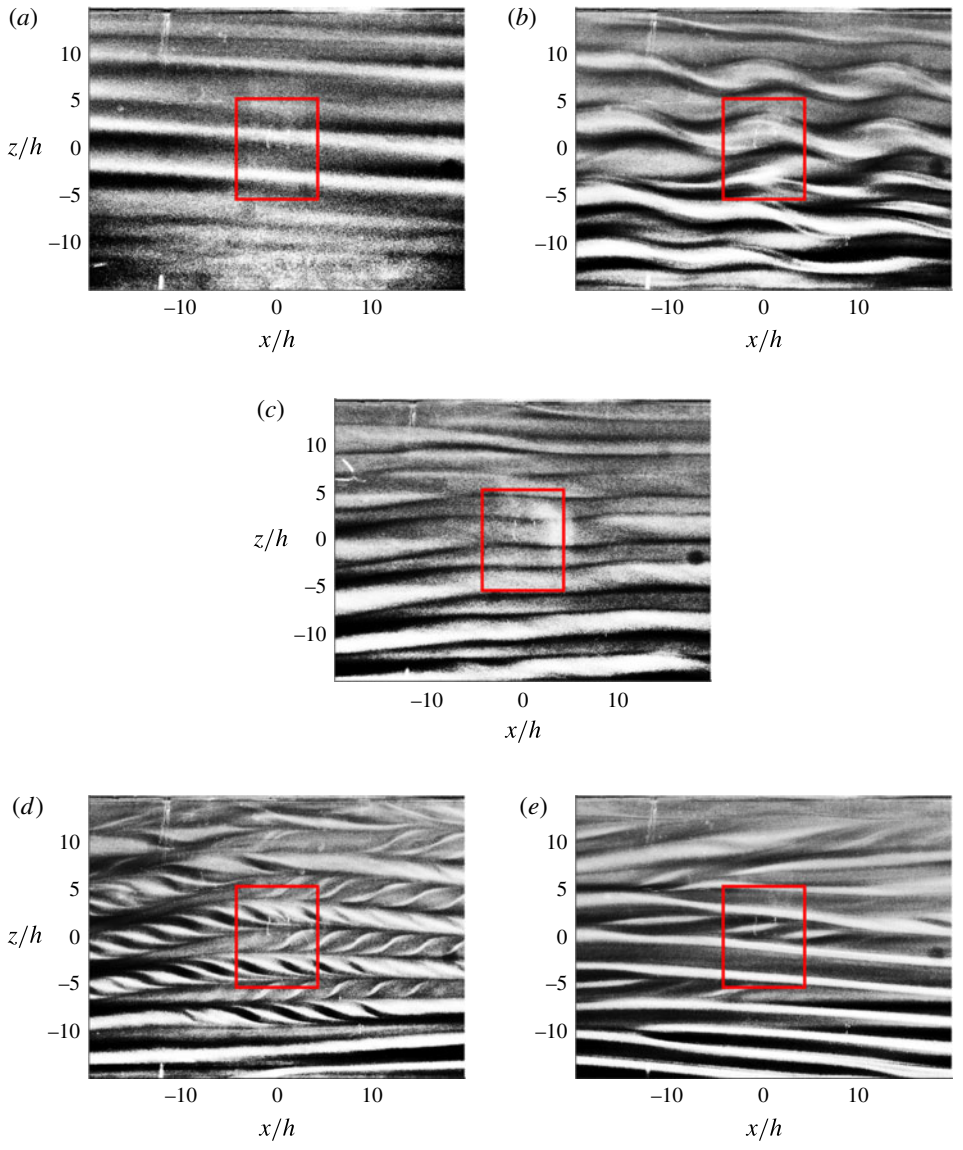


FIGURE 3. (Colour online) Visualisation of the coherent roll-cell structure at $Re = 100$ and some selected rotation numbers: (*a*) $\Omega = 1.5$, (*b*) $\Omega = 8$, (*c*) $\Omega = 20$, (*d*) $\Omega = 55$, (*e*) $\Omega = 90$. The red rectangle shown in each figure is roughly presenting the location and size of the PIV measurement domain.

a remarkable fluid motion in the wall-normal direction, as shown by the red/black arrows in figure 4(*c*). In fact, as will be presented in the next section, the 2Dh roll cells cause the largest momentum transport in the wall-normal direction among the various Ω cases studied.

With further increase of the rotation number the roll-cell structure takes more complex forms. At $\Omega = 55$ the roll cells show oblique stripes, as shown in figure 3(*d*). This structure is named twisted roll cell and has been observed in earlier experiments

https://doi.org/10.1017/jfm.2016.57 Published online by Cambridge University Press

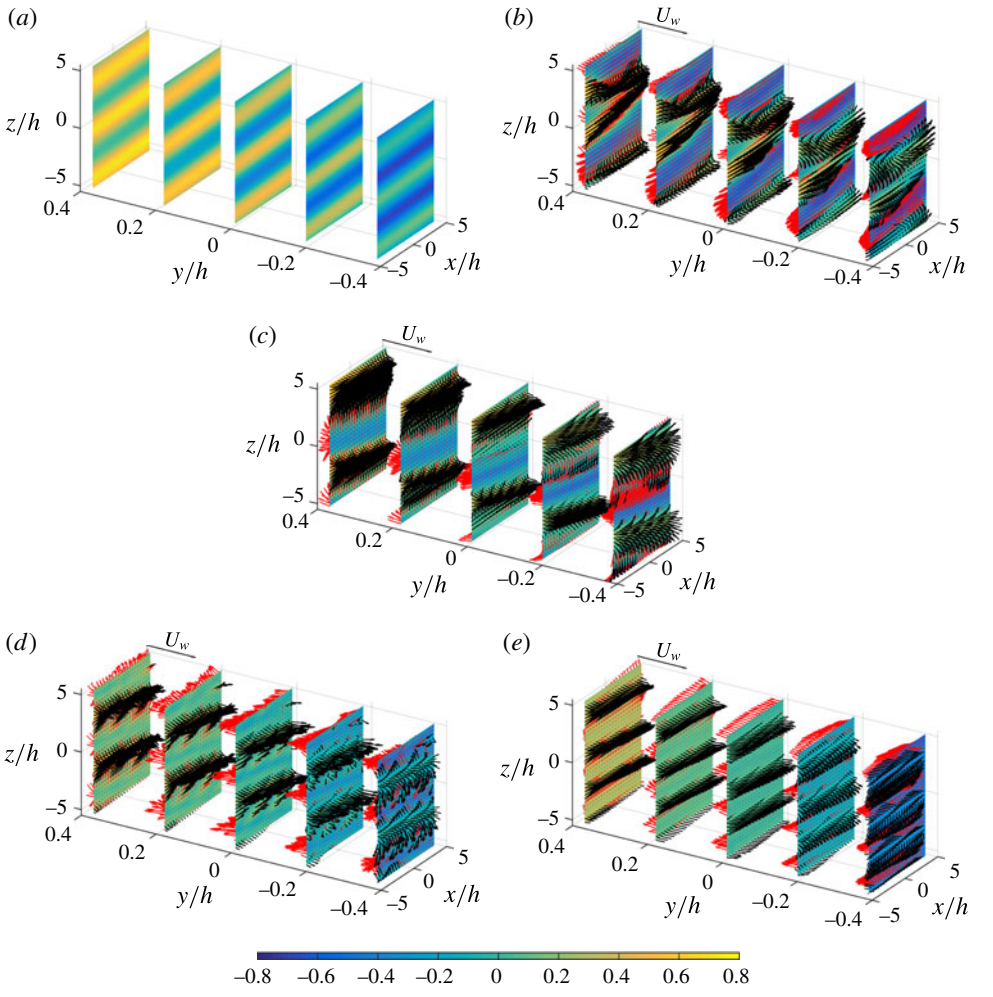


FIGURE 4. (Colour online) Instantaneous velocity fields measured by stereoscopic PIV at the same Reynolds number ($Re = 100$) and rotation numbers as in figure 3: (*a*) $\Omega = 1.5$, (*b*) $\Omega = 8$, (*c*) $\Omega = 20$, (*d*) $\Omega = 55$, (*e*) $\Omega = 90$. The colour shows the value of the instantaneous streamwise velocity component $\tilde{u}/U_w$, and the red/black arrows present velocity vectors with positive/negative wall-normal velocity. A black arrow showing the length of U_w is also shown at the left top of each figure.

(Suryadi *et al.* 2014). The stripes of the twisted roll-cell structure can also be seen by the velocity vector pattern in figure 4(*d*).

At $\Omega = 90$ (figure 3*e*) the roll-cell structure, which is streamwise-oriented and fairly straight, is much more complex than the straight roll cells observed at $\Omega = 1.5$ and $\Omega = 20$. This corresponds to the braided roll cells observed by Suryadi *et al.* (2014), and a recent numerical study (Daly *et al.* 2014) also found this braided roll-cell structure. While Suryadi *et al.* (2014) reported two different structures at $Re = 100$ and $\Omega = 90$, i.e. braided and staggered roll cells, only the braided-type structure was observed in both the stereoscopic PIV measurements and the flow visualisations in the present study. The corresponding instantaneous velocity field is

https://doi.org/10.1017/jfm.2016.57 Published online by Cambridge University Press

shown in figure 4(*e*). It should be noted that at $\Omega = 90$ the colour indicating the streamwise velocity component shows much less variation in the spanwise direction at each y-position compared with the other rotation number cases, which indicates that the streamwise velocity profile across the channel at this rotation number is close to that of the undisturbed laminar plane Couette flow without system rotation.

In figure 4 the red/black arrows shown at $\Omega = 8$, 20, 55 and 90 clearly indicate a significant fluid motion in the wall-normal direction induced by the roll-cell structures. In particular, $\Omega = 55$ is the case where the largest magnitude of the wall-normal velocity was observed, although the maximum momentum transport was observed at $\Omega = 20$. The magnitude of $\tilde{v}$ at $\Omega = 55$ is on average as large as 20 % of the wall speed U_w at the channel centre. It is also noteworthy that at $\Omega = 90$ the magnitude of $\tilde{v}$ is comparable to that at $\Omega = 55$, although the streamwise velocity $\tilde{u}$ is almost constant at each y-position. The wall-normal velocity component is generally in the range of $-0.3 \leqslant \tilde{v}/U_w \leqslant 0.3$, which agrees fairly well with the results of Daly *et al.* (2014).

4.2. *Mean flow profiles and zero-absolute-vorticity state*

In the present study the averaging operation is defined as taking the average in the streamwise and spanwise directions and in time as stated in § 2. Hence, the mean velocity U_i and the Reynolds stresses $\langle u_i u_j \rangle$ were evaluated as

$$U_i(y) = \frac{1}{N_t N_x N_z} \sum_{l=1}^{N_x} \sum_{m=1}^{N_z} \sum_{n=1}^{N_t} \tilde{u}(x_l, z_m, t_n; y), \tag{4.1}$$

$$\langle u_i u_j \rangle(y) = \frac{1}{N_t N_x N_z} \sum_{l=1}^{N_x} \sum_{m=1}^{N_z} \sum_{n=1}^{N_t} u_i(x_l, z_m, t_n; y) u_j(x_l, z_m, t_n; y), \tag{4.2}$$

where $u_i = \tilde{u}_i - U_i$ and N_x, N_z and N_t are the numbers of data points in the x- and z-directions and in time.

4.2.1. *Mean velocity, absolute vorticity and Reynolds stresses*

Mean flow profiles across the channel are presented in figure 5 at six representative rotation numbers (in total, measurements were made at 14 rotation numbers in the range $0 \leqslant \Omega \leqslant 106$). Figures 5(*a*) and 5(*b*) show the profiles of the mean streamwise velocity U/U_w and their deviation from the linear velocity profile $\Delta = U/U_w - y/h$ respectively. Figure 5(*c*) shows the corresponding profiles of the Reynolds shear stress $-\langle uv \rangle$, which physically represents the transport of the mean streamwise momentum by the wall-normal velocity. It is shown in these figures that as Ω increases from 1.5 to 20, the U profile increasingly deviates from the linear velocity profile (shown by the dashed line) and that the velocity gradient at the channel centre decreases (the slope of the profile at the channel centre gets closer to that of the dotted line).

The Reynolds shear stress $-\langle uv \rangle$ is obviously responsible for this change in the profile of U: $-\langle uv \rangle$ increases as the rotation number increases up to $\Omega = 20$, and has a maximum value at the channel centre at Ω around 20, which means that the 2Dh roll cells in figures 3(*c*) and 4(*c*) result in a significant momentum transport. However, in the higher rotation number range $-\langle uv \rangle$ decreases as the rotation number increases, and corresponding to this the profiles of U return towards the linear velocity profile. At $\Omega = 90$ the U profile is quite close to the linear velocity profile, although there still exist clear coherent roll cells, as shown in figure 3(*e*).

https://doi.org/10.1017/jfm.2016.57 Published online by Cambridge University Press

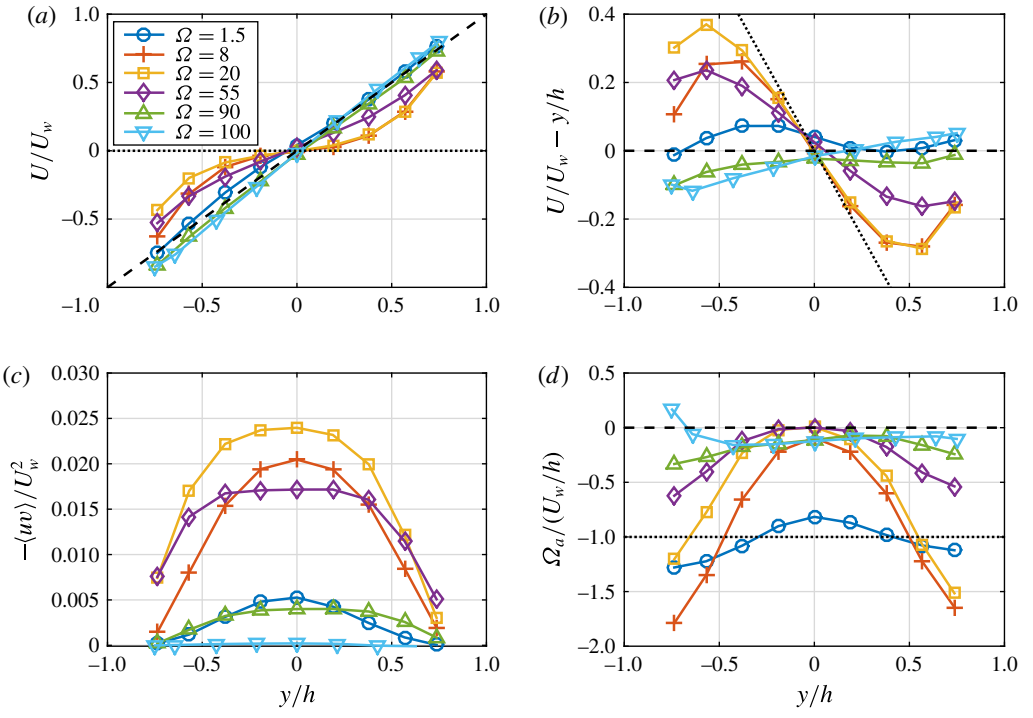


FIGURE 5. (Colour online) Mean flow profiles across the channel at $Re = 100$ and six different rotation numbers: (*a*) mean streamwise velocity U scaled by the wall speed U_w, (*b*) deviation from the linear velocity profile $U/U_w - y/h$, (*c*) Reynolds shear stress $-\langle uv\rangle$ scaled by U_w^2, (*d*) absolute vorticity scaled by U_w/h. The dashed and dotted lines in (*a*) and (*b*) show the linear velocity profile $U/U_w = y/h$ and $U = 0$ respectively, and those in (*d*) show $\Omega_a = 0$ and $\Omega_a = -U_w/h$, corresponding to the zero-absolute-vorticity state and the linear velocity profile with no system rotation.

Figure 5(*d*) presents the profiles of the absolute vorticity $\Omega_a = -\mathrm{d}U/\mathrm{d}y + 2\Omega_z$ evaluated from the U profiles shown in figure 5(*a*). In the case of no system rotation, the absolute vorticity is $-U_w/h$ across the channel, which is shown by the dotted line in the figure. It is seen that as the rotation number increases, the profile of Ω_a shifts from $\Omega_a = -U_w/h$ towards $\Omega_a = 0$ in the central part of the channel. The state of zero absolute vorticity is achieved at the channel centre at $\Omega = 20$, and the spatial extent of the region of the zero-absolute-vorticity state increases as the rotation number increases. At $\Omega = 100$ the absolute vorticity is close to zero across the full width of the channel.

Figure 6 presents the normal Reynolds stresses at the same rotation numbers as in figure 5. At $\Omega = 1.5$ the straight roll cells, as shown in figure 4(*a*), give rise to a significant streamwise velocity variation, and the maximum value at the channel centre is approximately $0.08U_w^2$, which corresponds to a root mean square variation of 28 % of the wall speed U_w. On the other hand, the lateral stress components are almost zero at this rotation number. However, as the rotation number increases, $\langle u^2\rangle$ generally decreases and $\langle v^2\rangle$ and $\langle w^2\rangle$ increase. In particular, $\langle u^2\rangle$ at the channel centre rapidly decreases and the profile of $\langle u^2\rangle$ changes into an 'M'-type shape. In contrast, $\langle v^2\rangle$ always has its maximum value at the channel centre.

https://doi.org/10.1017/jfm.2016.57 Published online by Cambridge University Press

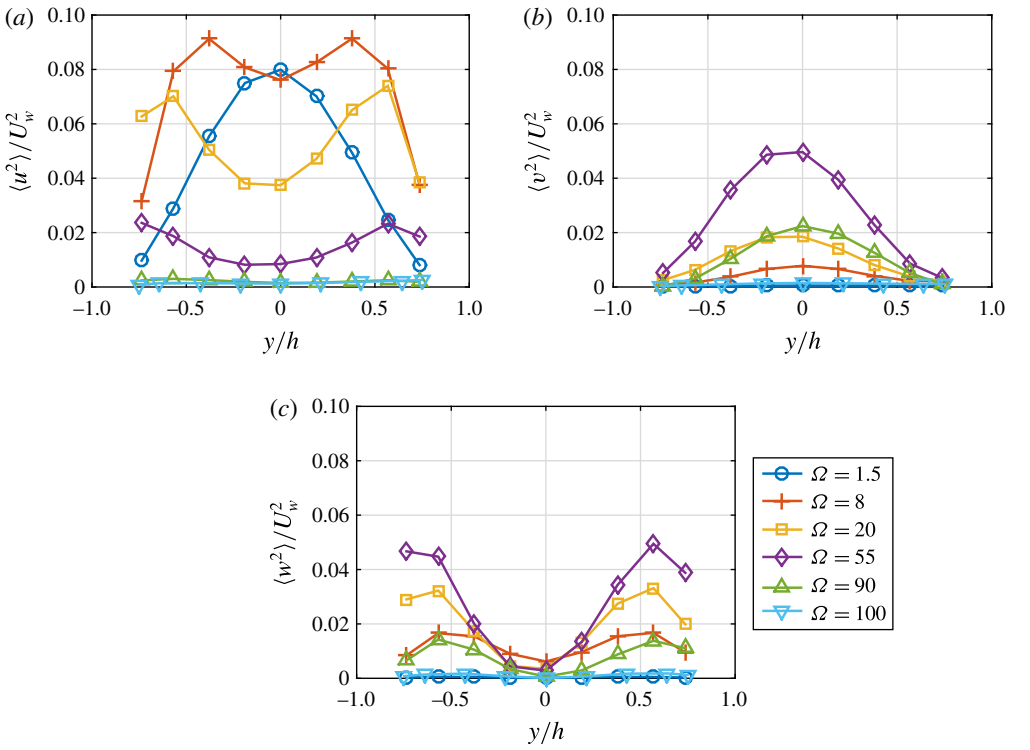


FIGURE 6. (Colour online) Profiles of the Reynolds normal stresses across the channel at $Re = 100$ and the same values of Ω as in figure 5: (*a*) $\langle u^2\rangle$, (*b*) $\langle v^2\rangle$, (*c*) $\langle w^2\rangle$. All stresses are scaled by U_w^2.

At $\Omega = 55$, where the twisted roll cells exist, as shown in figures 3(*d*) and 4(*d*), $\langle v^2\rangle$ and $\langle w^2\rangle$ show the largest magnitudes, and their maximum values are considerably larger than the streamwise component $\langle u^2\rangle$. In spite of the largest secondary fluid motion, the momentum transport by the roll cells at this rotation number, i.e. the Reynolds shear stress, is not the largest, which is mainly due to the small streamwise velocity variation $\langle u^2\rangle$. It is also noteworthy that at $\Omega = 90$, the values of $\langle v^2\rangle$ and $\langle w^2\rangle$ are still significant despite $\langle u^2\rangle$ being almost zero, which corresponds to the characteristics of the instantaneous velocity field shown in figure 4(*e*). Such behaviour of the Reynolds shear stress and the anomalous balance between the Reynolds normal stresses will be further discussed based on their production term in § 5.

4.2.2. *Wall shear stress variation with system rotation rate*

The wall shear stress can be seen as a measure of momentum exchange in the wall-normal direction by viscous diffusion and the Reynolds shear stress, and is therefore also strongly connected with the momentum transport caused by the roll-cell structure. Although a direct evaluation of the wall shear stress is generally not possible based on PIV measurement data, it is possible in the present study because of the constant total-shear-stress profile in the plane Couette flow configuration, as indicated by (2.9). Figure 7(*a*) presents an example of the viscous, Reynolds and total shear stresses scaled by ρU_w^2 measured at $\Omega = 8$. It is demonstrated that the evaluated total stress is fairly constant throughout the channel as it theoretically should be (see (2.8)), which

https://doi.org/10.1017/jfm.2016.57 Published online by Cambridge University Press

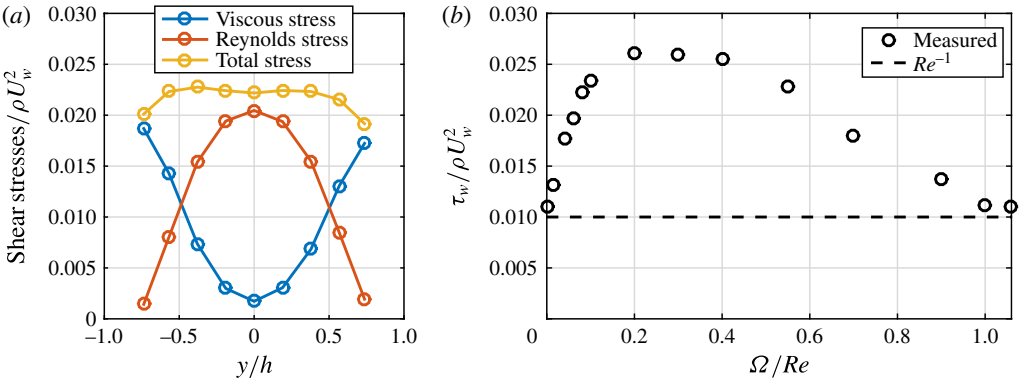


FIGURE 7. (Colour online) Indirect evaluation of wall shear stress: (*a*) viscous, Reynolds and total shear stresses evaluated based on stereoscopic PIV measurement results at $\Omega = 8$ and $Re = 100$; (*b*) variation of the evaluated wall shear stress with Ω/Re (the dashed line shows the value in the case of no rotation, Re^{-1}).

supports the validity of the present measurement results. The wall shear stress τ_w was determined by taking the average of the total stress for the measurement points in the interval $-0.57 \leqslant y/h \leqslant 0.57$.

The evaluated wall shear stress τ_w scaled by ρU_w^2 is shown in figure 7(*b*). The theoretical value of $\tau/\rho U_w^2$ in the case of the linear velocity profile, which is given by (2.11), is also shown by the dashed line for comparison. The wall shear stress τ_w increases from Re^{-1} at $\Omega = 0$, and takes a maximum at $\Omega = 20$, corresponding to the behaviour of the Reynolds shear stress $-\langle uv \rangle$. The peak value of τ_w at $\Omega = 20$ is 0.026, more than twice the value of the $\Omega = 0$ case, which indicates significant momentum transport induced by the roll-cell structure. In the higher rotation number range τ_w decreases towards the theoretical value of the linear velocity profile case, as Ω approaches 100.

4.2.3. *Zero-absolute-vorticity state in scaling by friction velocity*

The focus is now set on the connection between the Reynolds shear stress $-\langle uv \rangle$ and the absolute vorticity $\Omega_a = -\mathrm{d}U/\mathrm{d}y + 2\Omega_z$ at the channel centre. As the wall shear stress is evaluated in § 4.2.2, scaling of the experimental results based on the friction velocity $u_\tau = \sqrt{\tau_w/\rho}$ is possible. In this scaling the absolute vorticity is written as

$$\Omega_a^+ = \frac{\Omega_a}{u_\tau^2/\nu} = -\frac{\mathrm{d}U^+}{\mathrm{d}y^+} + \Omega_\tau, \tag{4.3}$$

where Ω_τ is the system rotation rate scaled by u_τ: $\Omega_\tau = 2\Omega_z \nu/u_\tau^2$. This scaling with u_τ has the clear advantage that the sum of the mean velocity gradient and the Reynolds shear stress is always constant and equal to unity throughout the channel:

$$\frac{\mathrm{d}U^+}{\mathrm{d}y^+} - \langle uv \rangle^+ = 1, \tag{4.4}$$

which makes the connection between the Reynolds shear stress and the absolute vorticity clearer. Equations (4.3) and (4.4) immediately give us the variation of

https://doi.org/10.1017/jfm.2016.57 Published online by Cambridge University Press

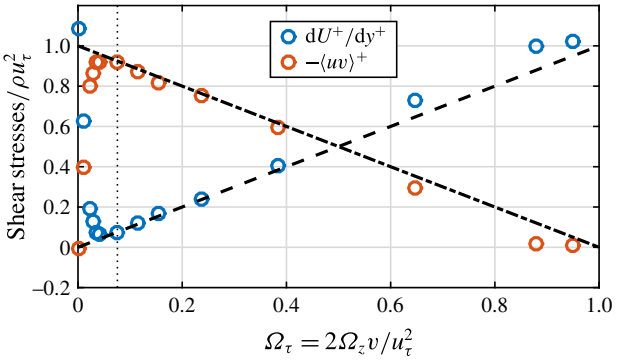


FIGURE 8. (Colour online) Mean streamwise velocity gradient $\mathrm{d}U^+/\mathrm{d}y^+$ and Reynolds shear stress $-\langle uv\rangle^+$ at the channel centreline. The vertical dotted line shows the value of $\Omega_\tau = 0.076$ corresponding to $\Omega = 20$, and the dashed and chain lines indicate $\mathrm{d}U^+/\mathrm{d}y^+ = \Omega_\tau$ and $-\langle uv\rangle^+ = 1 - \Omega_\tau$ respectively, corresponding to the zero-absolute-vorticity state.

$\mathrm{d}U^+/\mathrm{d}y^+$ and $-\langle uv\rangle^+$ with the rotation number under the state of zero absolute vorticity, $\Omega_a^+ = 0$:

$$\frac{\mathrm{d}U^+}{\mathrm{d}y^+} = \Omega_\tau, \tag{4.5}$$

$$-\langle uv\rangle^+ = 1 - \Omega_\tau. \tag{4.6}$$

The variation of the measured mean velocity gradient and the Reynolds shear stress at the channel centre is presented in figure 8 scaled by ρu_τ^2. It is shown that the Reynolds shear stress $-\langle uv\rangle^+$ rapidly increases from $-\langle uv\rangle^+ = 0$ to approximately 1 as the rotation number Ω_τ increases, and it begins to decrease following the chain line indicating the zero absolute vorticity, (4.6), at approximately $\Omega_\tau = 0.076$, corresponding to $\Omega = 20$. On the other hand, the mean velocity gradient $\mathrm{d}U^+/\mathrm{d}y^+$ rapidly decreases from 1 as the rotation number increases from zero to $\Omega_\tau = 0.076$ and then starts to increase for higher rotation numbers according to the zero-absolute-vorticity state range, satisfying (4.4).

In this section, some typical roll-cell structures of RPCF and mean flow profiles at $Re = 100$ and selected rotation numbers were presented. An anomalous balance between the Reynolds normal stresses was found in the relatively high rotation number range where the mean flow behaves as the state of zero absolute vorticity at the channel centre, and the connection between the zero-absolute-vorticity state and the Reynolds shear stress at the channel centre was shown by the scaling based on the wall shear stress. In the next section, the production of the different Reynolds stress components is discussed in order to further elucidate the anomalous behaviour of the Reynolds stresses and the mechanism that keeps the absolute vorticity at zero near the channel centre.

5. Discussion

5.1. *Production of Reynolds stresses and physical interpretation of them based on the displaced-particle argument*

The equations for the production for the Reynolds normal stress components $\langle u^2\rangle$ and $\langle v^2\rangle$ obtained from (2.16) and (2.17) are

https://doi.org/10.1017/jfm.2016.57 Published online by Cambridge University Press

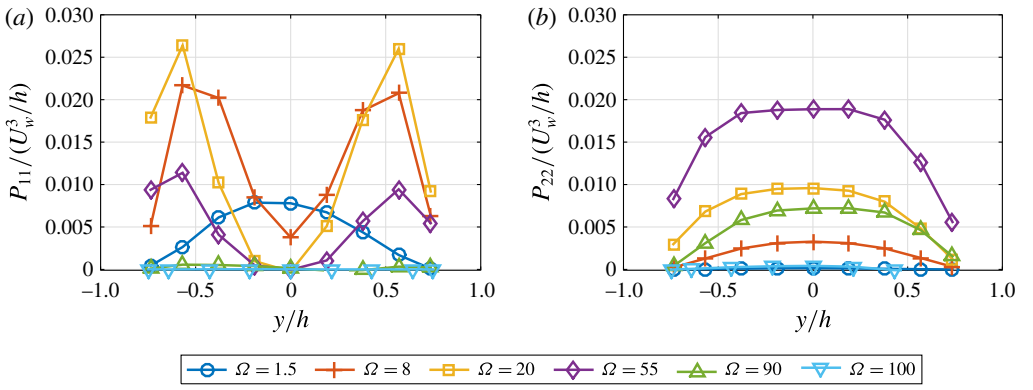


FIGURE 9. (Colour online) Production of the Reynolds normal stresses (*a*) $\langle u^2 \rangle$ and (*b*) $\langle v^2 \rangle$ scaled by U_w^3/h at $Re = 100$ and the same rotation numbers as shown in figure 5.

$$P_{11} = -2\langle uv \rangle \left(\frac{\mathrm{d}U}{\mathrm{d}y} - 2\Omega_z \right), \tag{5.1}$$

$$P_{22} = -4\langle uv \rangle \Omega_z, \tag{5.2}$$

and their profiles at several rotation numbers are presented in figures 9(*a*) and 9(*b*) respectively. It is shown that at $\Omega = 1.5$ the production of $\langle u^2 \rangle$ is large in the channel centre region, while the production of $\langle v^2 \rangle$ is almost zero across the entire channel. At $\Omega \geqslant 20$, P_{11} is almost zero at the channel centre, which is obviously because the velocity gradient $\mathrm{d}U/\mathrm{d}y$ and the system rotation $2\Omega_z$ in (5.1) cancel each other there due to the zero-absolute-vorticity state. Instead, P_{22} in the channel centre region increases as the rotation number increases. At $\Omega = 90$, P_{11} is close to zero across the channel, while P_{22} is still large, as can be understood from (5.2). The different behaviour of the production terms results in the anomalous balance between $\langle u^2 \rangle$ and $\langle v^2 \rangle$ shown in figure 6.

One can also explain the small streamwise velocity variation in the xz-plane at high Ω with a displaced-particle argument (similar to the Prandtl (1925) mixing length theory and used by Tritton & Davies (1985) to discuss stability of spanwise rotating shear flows). Consider a fluid particle moving in the streamwise direction with the local mean velocity $U(y)$ and perturbed to also move in the wall-normal direction with the wall-normal velocity v, i.e. the instantaneous local velocity $\tilde{\boldsymbol{u}}$ is perturbed from $\tilde{\boldsymbol{u}} = U(y)\boldsymbol{e}_1 + 0\boldsymbol{e}_2$ to $\tilde{\boldsymbol{u}} = U(y)\boldsymbol{e}_1 + v\boldsymbol{e}_2$. After a small duration Δt, the fluid particle has travelled a distance $v\Delta t$ in the y-direction, which gives rise to a streamwise velocity deficit

$$\Delta u = U(y) - U(y + v\Delta t) \approx -v\frac{\mathrm{d}U}{\mathrm{d}y}\Delta t. \tag{5.3}$$

However, at the same time the fluid particle is accelerated in the streamwise direction by the Coriolis force $2\Omega_z v$ during Δt. Therefore, the overall velocity deficit due to the fluid displacement in the y-direction is

$$\Delta u = -v\frac{\mathrm{d}U}{\mathrm{d}y}\Delta t + 2\Omega_z v\Delta t = -v\left(\frac{\mathrm{d}U}{\mathrm{d}y} - 2\Omega_z \right)\Delta t, \tag{5.4}$$

which clearly shows that under the state of zero absolute vorticity, i.e. $-\mathrm{d}U/\mathrm{d}y + 2\Omega_z = 0$, the motion of the fluid particle in the y-direction does not result in any

https://doi.org/10.1017/jfm.2016.57 Published online by Cambridge University Press

streamwise velocity variation. It should be noted that by multiplying both sides of (5.4) by u and applying the averaging operation one obtains

$$\Delta\langle u^2\rangle = -2\langle uv\rangle\left(\frac{\mathrm{d}U}{\mathrm{d}y} - 2\Omega_z\right)\Delta t. \tag{5.5}$$

Thus, the explanation given above shows the physical process in which the production of the streamwise velocity variation $\langle u^2\rangle$ occurs.

Equation (5.4) suggests that the wall-normal fluid motion induces two different effects on the streamwise momentum transport which are conflicting each other. One is the fluid mixing effect, which is represented by the term associated with the mean velocity gradient, and the other is the streamwise Coriolis acceleration, and one can see that the Coriolis acceleration enhances the velocity variation across the channel (i.e. in the y-direction), in contrast to the fluid mixing effect, which acts to make the velocity distribution uniform; the sign of the Coriolis term $2\Omega_z v$ is always the same as that of v (for $\Omega_z > 0$), which means that the fluid particles moving towards the top wall ('top' referring to figure 1) of the channel are accelerated in the positive x-direction, while those moving towards the bottom wall are accelerated in the negative x-direction. Therefore, the zero absolute vorticity is a state where these two conflicting effects are in balance.

With regard to the shear stress, the production of $-\langle uv\rangle$ is

$$P_{12} = \underbrace{2\langle u^2\rangle\Omega_z}_{\mathrm{I}} + \underbrace{\langle v^2\rangle\left(\frac{\mathrm{d}U}{\mathrm{d}y} - 2\Omega_z\right)}_{\mathrm{II}}, \tag{5.6}$$

and the terms I and II are the contributions from the streamwise and wall-normal velocity variations respectively. The production P_{12} itself is presented in figure 10(a), and the contributions from the terms I and II are separately shown in figures 10(b) and 10(c). The profile of P_{12} has a minimum at the channel centre and maxima at approximately $y/h = \pm 0.5$, and shows the largest magnitude at $\Omega = 20$. Thus, the Reynolds shear stress is largest at this rotation number. Comparing the contribution from each term in (5.6) shown in figure 10(b,c), one can clearly see that the second term II is generally small compared with the first term I throughout the channel even at $\Omega = 55$, in spite of the considerable wall-normal velocity fluctuation $\langle v^2\rangle$. This is because at the channel centre the velocity gradient and system rotation effect cancel each other due to the zero-absolute-vorticity state, and in the near-wall region $\langle v^2\rangle$ itself decreases (see the profile of $\langle v^2\rangle$ in figure 6b). Thus, the contribution to the production P_{12} is mainly from the term I regardless of the rotation number, and the strong wall-normal fluid motion observed at relatively high rotation numbers does not contribute to the production of $-\langle uv\rangle$.

Furthermore, in order to directly compare such behaviour of P_{12} with $\langle uv\rangle^+$ at the channel centre shown in figure 8, P_{12} is now scaled by u_τ^4/ν and decomposed into three terms as

$$P^+_{-uv} = \underbrace{\langle u^2\rangle^+\Omega_\tau}_{\mathrm{i}^+} + \underbrace{\langle v^2\rangle^+\frac{\mathrm{d}U^+}{\mathrm{d}y^+}}_{\mathrm{ii}^+} + \underbrace{\left(-\langle v^2\rangle^+\Omega_\tau\right)}_{\mathrm{iii}^+}, \tag{5.7}$$

in order to look into the balance between them in more detail. The values of each term at the channel centre are compared in figure 11(a), and as before the terms ii^+ and iii^+ generally cancel each other, but their magnitude is larger than the first term i^+. A zoomed view of the variation of the term i^+ is shown in figure 11(b), where it can be seen that the term i^+ rapidly increases as the rotation number increases at low

https://doi.org/10.1017/jfm.2016.57 Published online by Cambridge University Press

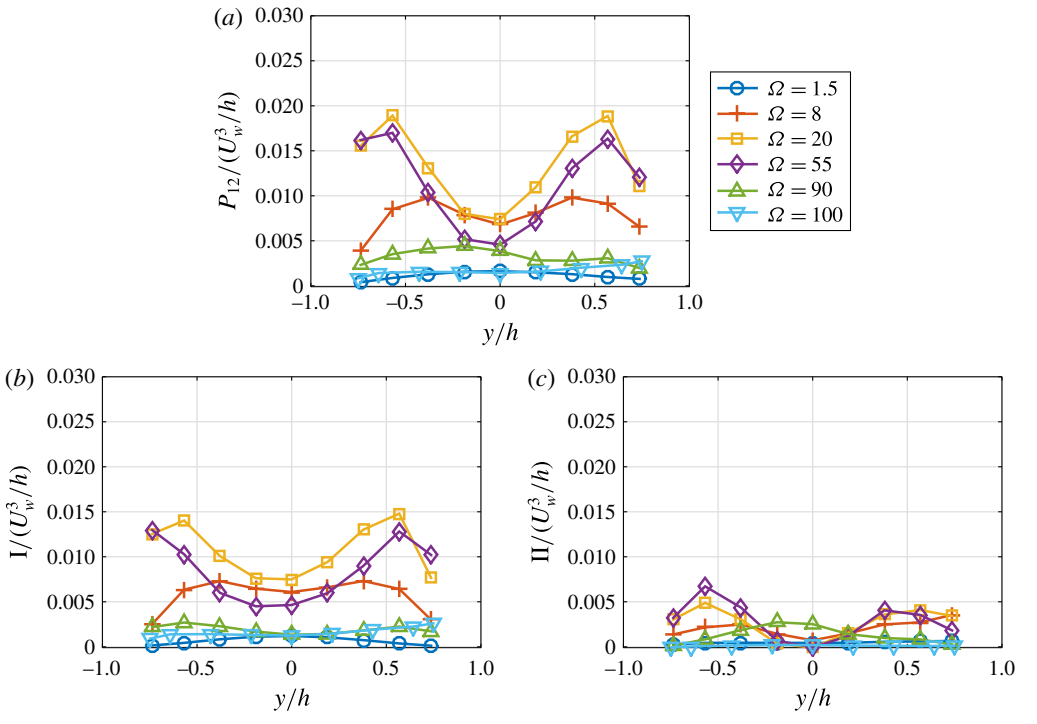


FIGURE 10. (Colour online) Production of the Reynolds shear stress $-\langle uv\rangle$ and the first and second terms in (5.6) scaled by U_w^3/h at $Re = 100$ and the same rotation numbers as shown in figure 5: (*a*) P_{12} itself, (*b*) the term I, (*c*) the term II.

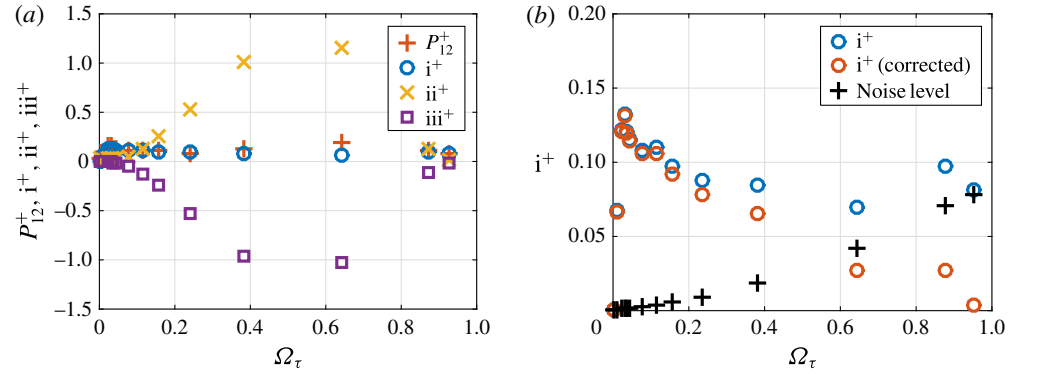


FIGURE 11. (Colour online) Production terms of $-\langle uv\rangle$ scaled by u_τ^4/ν, P_{12}^+, at the channel centre: (*a*) comparison of P_{12}^+ itself and all three terms in (5.7); (*b*) the term i$^+$.

rotation numbers, but in the higher rotation number range it generally decreases. This behaviour of the term i$^+$ results in the variation of $-\langle uv\rangle^+$ shown in figure 8.

It should also be mentioned that P_{12} at $\Omega = 100$ shown in figure 9(*a*) and the term i$^+$ at $\Omega_\tau = 0.88$ and 0.95 (corresponding to $\Omega = 100$ and 106 respectively) in figure 11(*b*) are not zero, although at these rotation numbers the flow should be stable.

https://doi.org/10.1017/jfm.2016.57 Published online by Cambridge University Press

This is due to overestimation of the term i^+ by the noise of the stereoscopic PIV measurement: as stated in § 3.2, the velocity measurement contains the measurement noise of 3 % of U_w, the influence of which on the evaluation of the term i^+ is larger at higher rotation numbers as it is multiplied by the rotation number. This noise effect and the term i^+ corrected by subtracting the noise effect are also shown in figure 11(*b*). It is shown that the corrected values of the term i^+ monotonically decrease towards zero as Ω_τ reaches 1, which well explains the behaviour of the Reynolds shear stress $\langle uv\rangle^+$ shown in figure 8.

The physical interpretation of the terms I and II of (5.6) is further discussed in the following. In a similar manner to that used to derive (5.4), let us consider that a fluid particle moving with an instantaneous velocity $\tilde{\boldsymbol{u}} = U(y)\boldsymbol{e}_1 + 0\boldsymbol{e}_2$ is perturbed in the streamwise direction, i.e. the local instantaneous velocity is perturbed to be $\tilde{\boldsymbol{u}} = (U(y) + u)\boldsymbol{e}_1 + 0\boldsymbol{e}_2$. Due to the velocity fluctuation u, an extra wall-normal Coriolis force $-2\Omega_z u$ is induced and accelerates the fluid particle in the y-direction, which gives a change in the wall-normal velocity component,

$$\Delta v = -2\Omega_z u \Delta t, \tag{5.8}$$

after a short time Δt. By multiplying (5.8) by u and (5.4) by v, and applying the averaging operation, we obtain

$$-\langle u\Delta v\rangle = 2\Omega_z\langle u^2\rangle\Delta t, \tag{5.9}$$

$$-\langle v\Delta u\rangle = \langle v^2\rangle\left(\frac{\mathrm{d}U}{\mathrm{d}y} - 2\Omega_z\right)\Delta t. \tag{5.10}$$

These two expressions obviously correspond to terms I and II of (5.6) respectively, and we can easily reproduce the production of $-\langle uv\rangle$ by taking the sum of them:

$$-\langle v\Delta u\rangle - \langle u\Delta v\rangle = \Delta(-\langle uv\rangle) = \left[2\Omega_z\langle u^2\rangle + \langle v^2\rangle\left(\frac{\mathrm{d}U}{\mathrm{d}y} - 2\Omega_z\right)\right]\Delta t. \tag{5.11}$$

Now it is clear that the terms I and II in (5.6) represent different physical processes in which the streamwise momentum transport in the wall-normal direction is enhanced. The term I represents the process such that a streamwise velocity variation induces an extra wall-normal Coriolis force that accelerates the fluid particle in the wall-normal direction, by which momentum transport is produced. On the other hand, the term II represents the effects of the wall-normal fluid motion on the momentum transport: the momentum transport in the wall-normal direction driven by the secondary fluid motion of the roll-cell structure and the streamwise Coriolis acceleration that compensates it, as already discussed above.

These two effects induced by the wall-normal fluid motion, which are represented by the term II of (5.6), are quite significant but conflict each other, as shown in figure 11(*a*) (terms ii^+ and iii^+), and the sum of them is zero under the zero-absolute-vorticity state.

5.2. *Mechanism for maintaining the state of zero absolute vorticity*

The mechanism by which the absolute vorticity is maintained zero at the channel centre is now addressed based on the Reynolds stress production. Let us assume that the mean velocity gradient at the channel centre is slightly deviated from the

https://doi.org/10.1017/jfm.2016.57 Published online by Cambridge University Press

zero-absolute-vorticity state by a small disturbance δ:

$$\frac{\mathrm{d}U}{\mathrm{d}y} = 2\Omega_z + \delta. \tag{5.12}$$

In this case, the equations for the production for the Reynolds stresses are

$$P_{11} = -2\langle uv\rangle\delta, \tag{5.13}$$

$$P_{22} = -4\langle uv\rangle\Omega_z, \tag{5.14}$$

$$P_{12} = 2\Omega_z\langle u^2\rangle + \langle v^2\rangle\delta. \tag{5.15}$$

One can clearly see by (5.13)–(5.15) that P_{11} and P_{12} are directly affected by the value of δ while P_{22} is not.

It can be seen from (5.15) that the second term of P_{12}, $\langle v^2\rangle\delta$, always affects the Reynolds shear stress $-\langle uv\rangle$ so that the mean flow profile returns to the zero-absolute-vorticity state. In the case of $\delta > 0$, the second term of P_{12} is no longer zero but positive, and hence P_{12} increases and so does $-\langle uv\rangle$, which eventually decreases the mean velocity gradient. In the same manner, if $\delta < 0$, $-\langle uv\rangle$ decreases as the second term of P_{12} turns negative, by which the velocity gradient increases. This contribution of the second term in (5.15) can be considered to be significant when the mean flow profile deviates from the zero-absolute-vorticity state, because the magnitude of the $\langle v^2\rangle$-related terms in P_{12} is remarkably larger than the first term, as already shown in figure 11(*a*).

In addition, P_{11} also supports the state of zero absolute vorticity through the first term of P_{12}, $2\langle u^2\rangle\Omega_z$. As shown in (5.13), in the case of $\delta > 0$, P_{11} becomes positive, and hence the first term of P_{12} eventually increases, which is favourable for the aforementioned work of the second term that maintains the zero absolute vorticity. On the other hand, in the case of $\delta < 0$, the second term of P_{12} is negative, as mentioned above, while the first term is always positive, and thus their contributions conflict each other. However, the contribution of the first term is weakened as $\langle u^2\rangle$ decreases, because the production P_{11} is negative due to $\delta < 0$. Thus, the first term of P_{12} always behaves favourably for the second term that maintains the zero-absolute-vorticity state.

6. Conclusion

The momentum transport caused by the roll-cell structure in laminar rotating plane Couette flow at $Re = 100$ was experimentally investigated by stereoscopic PIV measurements, and the mechanism of the state of zero absolute vorticity was discussed mainly based on the statistical quantities such as the Reynolds stresses and their production. It was revealed that the momentum transport is mainly caused by the wall-normal Coriolis acceleration induced by disturbance to the streamwise velocity component, and becomes the largest at the rotation number $\Omega = 20$, where the roll-cell structure takes the form of two-dimensional roll cells. At higher rotation numbers the mean flow adheres to a state of zero absolute vorticity in the channel centre region, and the roll-cell structure shows more complex forms, such as twisted roll cells and braided roll cells, which induce strong secondary fluid motion. Such fluid motion does not, however, directly contribute to the net momentum transport, because the momentum transport across the channel and the streamwise Coriolis acceleration, both of which are induced by the wall-normal fluid motion, cancel each other under the zero-absolute-vorticity state. It was also found that the zero-absolute-vorticity

https://doi.org/10.1017/jfm.2016.57 Published online by Cambridge University Press

state is maintained by a balance between the Reynolds shear-stress production terms associated with these two different effects by the wall-normal fluid motion. Therefore, it can be reasonably concluded that the strong wall-normal secondary fluid motion of the coherent roll-cell structure of RPCF induces significant momentum transport and at the same time a Coriolis acceleration which conflict each other, and the zero-absolute-vorticity state is a stable state where these two effects are in balance.

Acknowledgements

The present work is supported by the C. Tryggers foundation for scientific research providing support for the postdoctoral position of the first author. We also thank Drs A. Suryadi, N. Tillmark and R. Örlü for various contributions during this study.

REFERENCES

ALFREDSSON, P. H. & TILLMARK, N. 2005 Instability, transition and turbulence in plane Couette flow with system rotation. In *Proceedings of the IUTAM Symp., Non-Uniqueness of Solutions to the Navier–Stokes Equations and their Connection with Laminar–Turbulent Transition* (ed. T. Mullin & R. Kerswell), pp. 173–193. Springer.

ANDERECK, C. D., LIU, S. S. & SWINNEY, H. L. 1986 Flow regimes in a circular Couette system with independently rotating cylinders. *J. Fluid Mech.* **164**, 155–183.

BECH, K. H. & ANDERSSON, H. I. 1997 Turbulent plane Couette flow subject to strong system rotation. *J. Fluid Mech.* **347**, 289–314.

BRADSHAW, P. 1969 The analogy between streamline curvature and buoyancy in turbulent shear flow. *J. Fluid Mech.* **36**, 177–191.

COULIOU, M. & MONCHAUX, R. 2015 Large-scale flows in transitional plane Couette flow: a key ingredient of the spot growth mechanism. *Phys. Fluids* **27**, 034101.

DALY, C. A., SCHNEIDER, T. M., SCHLATTER, P. & PEAKE, N. 2014 Secondary instability and tertiary states in rotating plane Couette flow. *J. Fluid Mech.* **761**, 27–61.

DAVIAUD, F., HEGSETH, J. & BERGÉ, P. 1992 Subcritical transition to turbulence in plane Couette flow. *Phys. Rev. Lett.* **69**, 2511–2514.

HAGIWARA, Y., SAKAMOTO, S., TANAKA, M. & YOSHIMURA, K. 2002 PTV measurement on interaction between two immiscible droplets and turbulent uniform shear flow of carrier fluid. *Exp. Therm. Fluid Sci.* **26**, 245–252.

HIWATASHI, K., ALFREDSSON, P. H., TILLMARK, N. & NAGATA, M. 2007 Experimental observations of instabilities in rotating plane Couette flow. *Phys. Fluids* **19**, 048103.

KLOOSTERZIEL, R. C., ORLANDI, P. & CARNEVALE, G. F. 2007 Saturation of inertial instability in rotating planar shear flows. *J. Fluid Mech.* **583**, 413–422.

KRISTOFFERSEN, R. & ANDERSSON, H. I. 1993 Direct simulations of low-Reynolds-number turbulent flow in a rotating channel. *J. Fluid Mech.* **256**, 163–197.

LEZIUS, D. K. & JOHNSTON, J. P. 1976 Roll-cell instabilities in rotating laminar and turbulent channel flows. *J. Fluid Mech.* **77**, 153–175.

MALERUD, S., LØY, K. J. MÅ & GOLDBURG, W. I. 1995 Measurements of turbulent velocity fluctuations in a planar Couette cell. *Phys. Fluids* **7**, 1949–1955.

NAGATA, M. 1998 Tertiary solutions and their stability in rotating plane Couette flow. *J. Fluid Mech.* **358**, 357–378.

PRANDTL, L. 1925 Über die ausgebildete Turbulenz. *Z. Angew. Math. Mech.* **5**, 136–138.

SOLOFF, S. M., ADRIAN, R. J. & LIU, Z.-C. 1997 Distortion compensation for generalized stereoscopic particle image velocimetry. *Meas. Sci. Technol.* **8**, 1441–1454.

SURYADI, A., SEGALINI, A. & ALFREDSSON, P. H. 2014 Zero absolute vorticity: insight from experiments in rotating laminar plane Couette flow. *Phys. Rev.* E **89**, 033003.

SURYADI, A., TILLMARK, N. & ALFREDSSON, P. H. 2013 Velocity measurements of streamwise roll cells in rotating plane Couette flow. *Exp. Fluids* **54**, 1617.

https://doi.org/10.1017/jfm.2016.57 Published online by Cambridge University Press

TANAKA, M., KIDA, S., YANASE, S. & KAWAHARA, G. 2000 Zero-absolute-vorticity state in a rotating turbulent shear flow. *Phys. Fluids* **12**, 1979–1985.

TILLMARK, N. & ALFREDSSON, P. H. 1991 An experimental study of transition in plane Couette flow. In *Advances in Turbulence 3* (ed. A. V. Johansson & P. H. Alfredsson), pp. 235–242. Springer.

TILLMARK, N. & ALFREDSSON, P. H. 1992 Experiments on transition in plane Couette flow. *J. Fluid Mech.* **235**, 89–102.

TILLMARK, N. & ALFREDSSON, P. H. 1996 Experiments on rotating plane Couette flow. In *Advances in Turbulence VI* (ed. S. Gavrilakis, L. Machiels & P. A. Monkewitz), pp. 391–394. Kluwer.

TRITTON, D. J. & DAVIES, P. A. 1985 Instabilities in geophysical fluid dynamics. In *Hydrodynamic Instabilities and the Transition to Turbulence*, 2nd edn. (ed. H. L. Swinney & J. P. Gollub), Topics in Applied Physics, vol. 45, pp. 229–270. Springer.

TSUKAHARA, T., TILLMARK, N. & ALFREDSSON, P. H. 2010 Flow regimes in a plane Couette flow with system rotation. *J. Fluid Mech.* **648**, 5–33.

WERELEY, S. & GUI, L. 2003 A correlation-based central difference image correction (CDIC) method and application in a four-roll mill flow PIV measurement. *Exp. Fluids* **34**, 42–51.

WILCOX, D. C. 1993 *Turbulence Modeling for CFD*. DCW Industries, Inc.

XIA, Z., SHI, Y. & CHEN, S. 2016 Direct numerical simulation of turbulent channel flow with spanwise rotation. *J. Fluid Mech.* **788**, 42–56.

ZETTNER, C. M. & YODA, M. 2001 The circular cylinder in simple shear at moderate Reynolds numbers: an experimental study. *Exp. Fluids* **30**, 246–353.

https://doi.org/10.1017/jfm.2016.57 Published online by Cambridge University Press